A Theoretical and Experimental Investigation of a Transonic Projectile Flowfield

Charles J. Nietubicz*
U.S. Army Ballistic Research Laboratory/ARDC, Aberdeen Proving Ground, Maryland
George R. Inger†
West Virginia University, West Virginia
and
James E. Danberg‡
University of Delaware, Newark, Delaware

The transonic flowfield about a secant-ogive cylinder boattail with a turbulent boundary layer has been studied. A joint theoretical and experimental effort is presented which compares the results of a generalized axisymmetric Navier-Stokes code, a composite inviscid boundary-layer/shock interaction solution method, and experiment. The experimental longitudinal pressure distribution at $M=0.94$ and 0.97 at $\alpha=0$ deg are generally well predicted by both theoretical techniques although the Navier-Stokes solutions are shown to be superior in describing the details, such as upstream effects of expansion corners and the position and magnitude of minimum pressure regions. Both theoretical solutions predict the boundary-layer velocity profiles very well in all cases with the largest differences occurring just downstream of the boattail corner. Comparisons of displacement thickness and skin friction distributions are also presented.

Nomenclature

C_{f_x} = longitudinal skin friction coefficient
C_p = pressure coefficient, $=2(p-p_\infty)/\rho_\infty u_\infty^2$
D = diameter, $=20.19$ cm
$\hat{E},\hat{G}$ = flux vectors of transformed Navier-Stokes equation
$\hat{H}$ = η-invariant source vector
H_x = shape factor θ_x/δ_x^*
L = total model length
M_∞ = freestream Mach number
M_l = preshock Mach number
p = pressure
$\hat{q}$ = vector containing dependent variables
Re = Reynolds number
$\hat{S}$ = viscous flux vector
u = longitudinal velocity component
t = time
x,y,z = rectangular coordinates
x,r,θ = cylindrical coordinates
α = angle of attack
γ = ratio of specific heat
δ = boundary-layer thickness
δ_x^* = longitudinal displacement thickness
θ_x = longitudinal momentum thickness
ξ,ζ = transformed coordinates
τ = transformed time
ρ = density
ϕ = nondimensional perturbation potential

Subscripts

e = edge conditions
∞ = freestream condition

Presented as Paper 82-0101 at the AIAA 20th Aerospace Sciences Meeting, Orlando, Fla., Jan. 11-14, 1982; received Oct. 12, 1982; revision received April 13, 1983.

*Aerospace Engineer. Member AIAA.
†Professor, Department of Mechanical and Aerospace Engineering.
‡Consultant. Associate Fellow AIAA.

I. Introduction

THE aerodynamic characteristics of standard artillery shell from subsonic to supersonic speeds are of major concern in the design of new shell or modifications to existing ones. The possibility that a given shape may have to operate throughout a range of Mach numbers requires a detailed understanding of the flowfields associated with each Mach number. Modern computational techniques are now being applied to projectile shapes and the ability to compute the aerodynamics of shell for a wide range of Mach numbers and Reynolds numbers is becoming a reality. Significant accomplishments have been made in the supersonic regime where static and Magnus force coefficients have been computed for standard projectile configurations and compare well with experimental data.[1,2] Transonic flow, however, presents additional complexity for computational analysis. Figure 1 is a schlieren photo showing the shock pattern existing about a typical projectile shape at transonic velocity. The formation of shock waves, imbedded in the flowfield near the surface discontinuities, produces a severe change in the aerodynamic coefficients such as drag and pitching moment. For example, the drag for a projectile shape has been found to change by as much as 100% through a Mach number range of 0.95 to 0.97.[3] A change of this magnitude in the aerodynamics makes it essential to be able to understand and compute the features of the flowfield which contribute to this effect.

A concentrated theoretical and experimental research program has been ongoing at the U.S. Army Ballistic Research Laboratory in order to develop the predictive capabilities required for determining projectile aerodynamics. Supersonic computations using combined inviscid flowfield and boundary-layer techniques have been developed by Sturek et al.[1] for cone-cylinder and ogive-cylinder configurations. Recent results have been obtained in supersonic flow over a typical boattailed projectile by Schiff and Sturek[2] using modern computational tecniques for solving the parabolized thin-layer Navier-Stokes equations.

Inviscid transonic computational results have been obtained by Reklis et al.[4] for a secant-ogive-cylindrical boattail

shape. This work was then extended to include the viscous boundary layer and modeling of the shock/boundary-layer interaction regions. A comparison of this composite solution technique with experimental data[5] showed generally good agreement.

A series of three-dimensional computations solving the thin-layer Navier-Stokes equations have been reported by Deiwert[6] for simulating afterbody flowfields. This excellent work was performed on the ILLIAC IV and allowed sufficient grid resolution in the boattail region to show the complicated flowfield structure which exists at angle of attack. The availability of these new computational techniques for solving the thin-layer generalized axisymmetric Navier-Stokes equations and additional experimental data has resulted in a continued analysis of this transonic flowfield problem. A discussion of the Navier-Stokes and composite computational methods and available experimental data will follow.

II. Generalized Axisymmetric Technique

The Navier-Stokes code which has been used in this study in the η-invariant or Generalized Axisymmetric version.[7] This code solves the thin-layer Navier-Stokes equations which are cast in strong conservation law form. The equation formulation allows for arbitrary body geometries and is solved using an implicit approximate factorization finite difference scheme. The "thin-layer" approximation[8-9] used here requires that all body surfaces be mapped onto $\zeta=$const planes and that $Re\gg 1$. Essentially all of the viscous terms in the coordinate directions (here taken as ξ and η) along the body surface are neglected while terms in the ζ or the near-normal direction to the body are retained. This approximation is used because, due to computer speed and storage limitations, fine grid spacing can only be provided in one coordinate direction (usually taken as the near-normal direction) and the grid spacing available in the other two directions is usually too coarse to resolve the viscous terms.

The thin-layer generalized axisymmetric Navier-Stokes equations are obtained from the three-dimensional equations by making use of two restrictions: 1) all body geometries are of an axisymmetric type and 2) the state variables and the contravariant velocities do not vary in the circumferential direction. Given the above assumptions the transformed generalized thin-layer Navier-Stokes equations in non-dimensional and strong conservation law form are written as[7]

$$\partial_\tau \hat{q}+\partial_\xi \hat{E}+\partial_\zeta \hat{G}+\hat{H}=Re^{-1}\partial_\zeta \hat{S} \qquad (1)$$

where general coordinate transformations

$\xi=\xi(x,y,z,t)$ longitudinal coordinate

$\zeta=\zeta(x,y,z,t)$ near-normal coordinate

$\tau=t$ time

are used.

The vector $\hat{q}$ contains the dependent variables, ρ, u, v, and w, and e. The vectors $\hat{E}$, $\hat{G}$, and $\hat{H}$ contain terms arising from the continuity equation, three momentum equations, and energy equation. All viscous terms are contained in the vector $\hat{S}$. The turbulence modeling used is the two-layer, Cebeci-type eddy-viscosity model as modified and reported by Baldwin and Lomax.[9]

Equation (1) contains only two spatial derivatives but does retain all three momentum equations, thus allowing a degree of generality over the standard axisymmetric equations. In particular, the circumferential velocity is not assumed to be zero, allowing computations for spinning projectiles or swirl flow to be accomplished.

The numerical algorithm used for Eq. (1) is a fully implicit, approximately factored finite difference scheme as analyzed by Beam and Warming.[10] The details of the numerical method, algorithm, and boundary conditions can be found in Ref. 7. The experiment was conducted in a continuous-flow tunnel, and thus, an adabatic wall boundary condition was used.

The numerical grid used for all the Navier-Stokes computations was generated using an elliptic solver[11] and is shown in Fig. 2. The computational region has been extended to four model lengths in front of and four model lengths behind the projectile. The far field boundary has been set at five model lengths. Such an extensive domain is used to eliminate the possibility of any wave reflection back on the model. The dark band of lines near the model surface results from a clustering of grid lines which are required in order to adequately resolve the boundary-layer region. The minimum spacing at the wall was 0.00002 model diameters, which

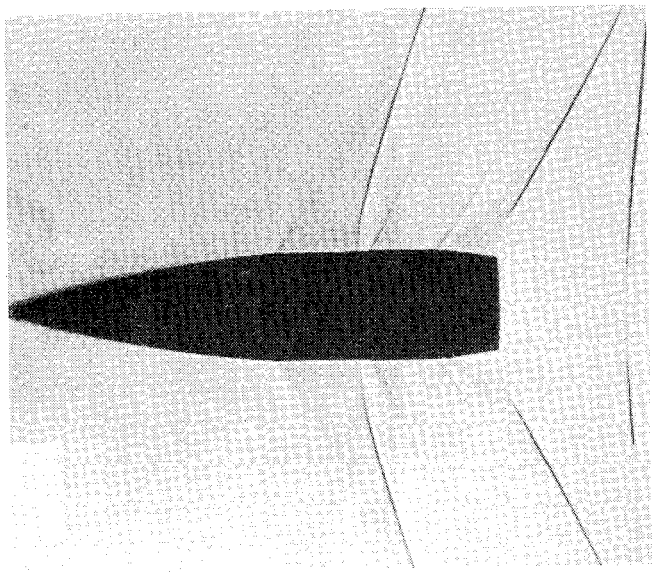

Fig. 1 Physical grid for Navier-Stokes computations.

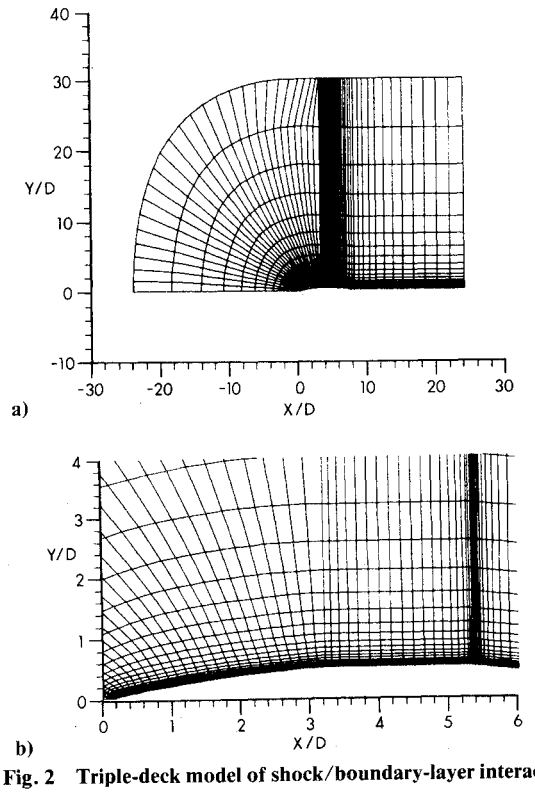

Fig. 2 Triple-deck model of shock/boundary-layer interaction.

resulted in at least 3-5 grid points being in the laminar sublayer. The total number of points in the normal direction was 40. There were 78 grid points in the longitudinal direction with clustering taking place at $X/D=3.2$ and 5.3, the ogive and boattail junction, respectively. No special clustering was applied to the shock/boundary-layer interaction region.

The projectile base was modeled as an extension of the 7.0 deg boattail for a distance of 2 calibers. The surface line was then turned parallel to the model axis for the remainder of the wake area. The base flow is thus modeled as an extended sting. A review of free-flight shadowgraphs for projectile shapes at transonic speeds does show the wake flow to follow near the boattail angle for a distance of 1-3 calibers before turning parallel to the flow direction.

III. Composite Inviscid Flow/Boundary-Layer/Shock Interaction Model

Inviscid Flow Region

The inviscid flow region is treated by the method developed by Reklis et al.[4] involving a numerical solution of the transonic small-disturbance equation for the velocity perturbation potential ϕ which, in cylindrical coordinates, is

$$[(1-M_\infty^2)-M_\infty^2(\gamma+1)\phi_x]\phi_{xx}+\phi_{rr}+\phi_r/r+\phi_{\theta\theta}/r^2=0 \quad (2)$$

The coordinates and ϕ are nondimensionalized by the freestream velocity and a characteristic dimension of the body. This equation is a second-order nonlinear partial differential equation of mixed elliptic-hyperbolic type. The type of equation changes to match the physical differences between regions of subsonic and supersonic flow.

Equation (2) generally yields adequate predictions of the inviscid flow about a projectile shape such as that studied here. Certain regions of the flow, however, require some modeling. The wake is simulated by a necked-down extension from the boattail base smoothly fared into a cylindrical sting over a distance of 2 calibers; the base flow is thus modeled as an extended sting similar to the Navier-Stokes computations. Of course the slip surface which physically exists is thus not accounted for in the calculations. Moreover, this obviously fails to account for the wake momentum defect and hence the base contribution to the overall drag. Additionally there is a slight overestimation of the pressure rise and hence the boundary-layer thickness growth and skin fricton drop near the end of the boattail, due to neglect of the correct base pressure upstream influence. However, for the present purposes where drag prediction is not of primary interest, these shortcomings are not deemed to be significant.

In order to develop a "conservative" algorithm to solve this equation special care must also be taken at transitions between subsonic and supersonic flow. Nonconservative forms of the algorithm, however, often given better agreement with experiment because the breakdown in conservation approximates the effect of shock obliquity resulting from shock/boundary-layer interaction [see Eq. (3)]. The algorithm used here was therefore a nonconservative one for the purposes of providing a first-order composite flow model. Consistently, first-order boundary condition relations have been used with 120 streamwise grid points along the body length with higher concentration in the corner and shock regions.

IV. Boundary Layer

Boundary-layer flow computations developed for laminar cone flows by Dwyer and Sanders,[12] were extended to more general turbulent flows by Sturek et al.[1] In this technique the boundary-layer equations for the conservation of mass, momentum, and energy are solved with an implicit finite difference technique. The solution begins with the development of an approximate boundary-layer profile at the tip. The solution is then marched over the body from nose to tail. At each step along the way a two-point boundary-value system is solved with conditions given at the body surface and at the boundary-layer edge. The possibility of body spin is accounted for and care is taken in setting up the difference to maintain stability. Turbulence is accounted for by use of an algebraic type, eddy viscosity, turbulent shear stress model with Van Driest damping. This model has proved suitable for use in cases of supersonic flow and is carried over directly to the transonic regime.

V. Local Shock/Boundary-Layer Interaction Regions

For nonseparating interactions (local Mach number roughly less than 1.3) in the Reynolds number range $10^6 \le Re_L \le 10^8$, a nonasymptotic triple-deck small-disturbance solution[13] of the weak normal shock/turbulent interaction is employed. This model has proven very successful in treating transonic interactions on supercritical airfoils including extensive experimetal verification[14]; its use therefore provides a sound treatment of both the local *and* downstream effects, while avoiding the use of crude empirical "viscous wedge" models whose fundamental dependence on the incoming boundary-layer properties is unknown.

The flow model (Fig. 3) consists of a double-decked region of mixed transonic inviscid rotational flow surrounding a shock discontinuity and an underlying thin shear stress disturbance sublayer within the law of the wall region that contains the upstream influence and skin friction perturbations. An approximate analytic solution is achieved by assuming small linearized disturbances ahead of and behind the nonlinear shock jump, with a simplified treatment of the detailed shock structure within the boundary layer down to the sonic level. The resulting equations can be solved by operational methods to obtain the interactive pressure rise, displacement thickness growth, and local skin friction solution both upstream and downstream of the shock foot (see Ref. 13 for details). This solution has been adapted to the present problem by an appropriate extension of the theory that considers the addition terms and effects due to the axisymmetric geometry.[15]

This interaction solution is used as a locally imbedded "interactive module" astride *each* of the *two* shock locations. The presence of a local compression shock abruptly terminating the local pockets of supersonic flow following both body corners is identified and located by the inviscid solution code and used to call the interaction solution as a interuptive subroutine centered about each such shock location, using the appropriate local preshock Mach number from the code as a driving input to the solution. When inserting the interaction we account for the fact that the nonconservative inviscid codes gives shock strengths slightly less than the full Rankine-Hugoniot normal shock jump assumed in the interaction solution. The preshock Mach number M_1 used in the latter solution is corrected to the value pertaining to a slightly oblique attached shock that produces maximum postshock flow deflection. This method, which is strongly supported by an interpretation of experimental evidence by numerous

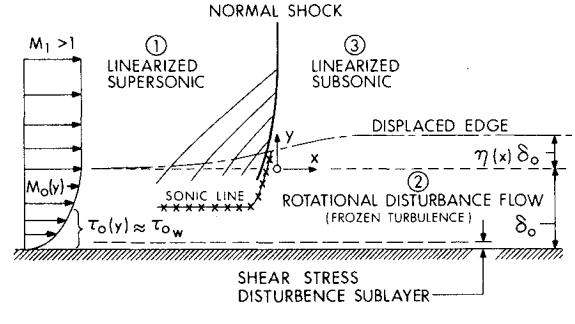

Fig. 3 Boattail model configuration.

investigators (see e.g., Refs. 14 and 16), yields

$$M_{1_{\text{eff}}} \simeq M_1 \sin(90 - 37.8\sqrt{M_1 - 1}) \quad (3)$$

The required inputs from the boundary-layer code are the local incoming displacement thickness and shape factor. The interaction subroutine replaces the boundary-layer code over the range of the interaction with a complete description (if desired) of the wall pressure, displacement thickness, and skin friction, plus the post-interaction values of δ^*, C_f and the (subsonic) inviscid edge conditions needed to restart the turbulent boundary-layer code. This method of introducing the interactive solution allows us to account not only for the rapid displacement thickness growth, but also for the attendant distortion of both the skin friction and profile shape. Moreover, the important influence of these changes on the subsequent boundary-layer development is included in the post-interaction reinitialization of the boundary-layer calculation. Consistent with the turbulent boundary-layer model employed within the interaction theory this reinitialization is carried out at the first station after the interation by means of the compressible version of Walz's general composite law of the wall-law of the wake velocity profile model.[17] The profile parameters are chosen to match final values of δ^*, C_f, and M_e given by the local interaction solution, while the wake function (hence, shape factor) automatically takes its consequent highly nonequilibrium post-shock value. Given this starting profile the turbulent boundary-layer code then marches downstream.

It is noted that since the shock locations here are essentially fixed by the sharp corners on the body and were found to alter only slightly due to viscous effects, there is no need to carry out a global interaction for their position as would be the case for supercritical airfoils; that is, to the present first-order approximation the shock strength and position may be taken from the inviscid calculation without the displacement thickness effect.

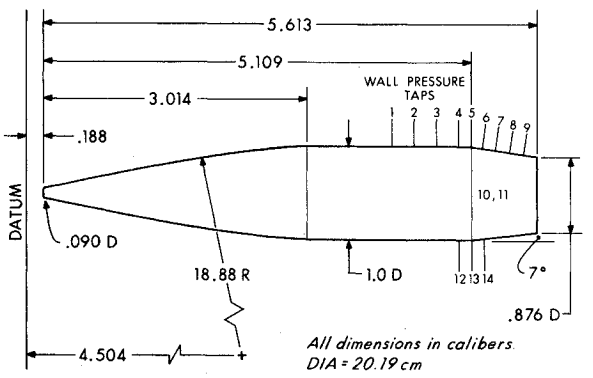

Fig. 4 Afterbody of wind tunnel model showing probe support mechanism.

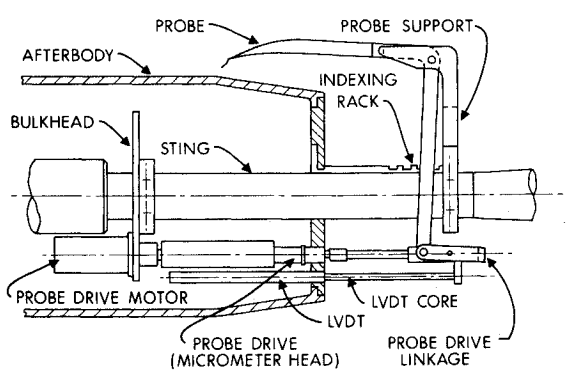

Fig. 5 Experimental comparison of Navier-Stokes, composite, and surface pressure coefficients; $M = 0.94$.

VI. Experiment

The experimental data to be described here are an extension of the data base reported in Ref. 18, including new tests at additional survey stations and at Mach number 0.97 as well as the previously reported data at a Mach number of 0.94.

The wind tunnel measurements were performed in the NASA Langley Research Center 8 ft Transonic Pressure Tunnel (TPT). The tunnel was operated at 1 atm supply pressure (101.3 kPa) and at supply temperature of 49.2°C, which resulted in a Reynolds number of 13×10^6 1/M. The TPT facility is of slotted wall construction to minimize reflected wave interference effects which were monitored using tunnel wall static pressure taps. The model was sting mounted from the Langley support sector and roll mechanism which allowed measurements at angle of attack and at various roll positions.

The data described here is limited to the zero angle of attack and roll case. Other experiments were performed at 4 deg angle of attack and at various angles around the model. Preliminary tests for pressure distributions and boundary surveys were additionally carried out on a nonconical afterbody model. The results from these tests will be reported in the near future.

VII. Model

The tests were made using a model of a typical modern projectile as illustrated in Fig. 4. The configuration is an idealization of an artillery projectile consisting of a secant-ogive nose, cylindrical midsection, and 7 deg conical afterbody (boattail) of a half a caliber. Turbulent flow was

Table 1 Experimental afterbody pressure distribution, $\alpha = 0$ deg

Tap	X/L	C_p $M_\infty = 0.94$	$M_\infty = 0.97$
1	0.805	−0.040	0.000
2	0.837	−0.054	−0.014
3	0.870	−0.068	−0.029
12	0.891	−0.107	−0.063
4	0.902	−0.165	−0.127
5	0.913	−0.535	−0.478
6	0.924	−0.542	−0.478
14	0.935	−0.505	−0.439
7	0.946	−0.472	−0.413
8	0.967	−0.314	−0.345
9	0.989	−0.036	−0.106
10	0.913	−0.523	−0.464
11	0.913	−0.561	−0.497
13	0.913	−0.561	−0.439
Base		−0.004	−0.005

Table 2 Measured boundary-layer characteristics, $\alpha = 0$ deg

X/L	δ, mm[a]	δ_x^*, mm[b]	θ_x, mm[b]	H_x
		$M_\infty = 0.94$		
0.869	10.94	1.74	0.99	1.75
0.902	11.53	1.68	1.97	1.73
0.924	13.22	1.33	0.75	1.78
0.946	11.57	1.39	0.74	1.88
0.968	12.59	2.05	1.07	1.92
0.989	13.97	2.79	1.44	1.94
		$M_\infty = 0.97$		
0.869	10.94	1.81	1.02	1.77
0.924	16.45	1.47	0.78	1.88
0.946	11.46	1.48	0.78	1.90
0.968	11.82	1.68	0.88	1.91
0.989	12.71	2.32	1.22	1.90

[a] δ based on $u/u_e = 0.995$. [b] δ_x^* and θ_x based on two-dimensional definitions.

$$\delta_x^* = \int_0^\delta \left(1 - \frac{\rho u}{\rho_e u_e}\right) dy, \quad \theta_x = \int_0^\delta \frac{\rho u}{\rho_e u_e}\left(1 - \frac{u}{u_e}\right) dy, \quad H_x = \frac{\delta_x^*}{\theta_x}$$

assured by using a stand-grain roughness strip 5 cm from the nose. The 20.2-cm-diam model caused 0.69% blockage of the tunnel which was found acceptable for the measurements carried out. The afterbody was instrumented with 14 static pressure taps located so as to define the flow conditions in the vicinity of the boattail corner.

VIII. Instrumentation

The boundary-layer surveys were made employing the same technique described in Ref. 5. The probing mechanism is shown in Fig. 5. Some new probe support arms were designed to increase the transvering distance of the probe tip to approximately 30 mm. This was found to be necessary on the leeside of the model during the previous tests. Separate probe supports were used to reach the various stations on the model and these were constructed so that all wall pressure tap stations on the model and these were constructed so that all wall pressure tap stations between 3 and 9 (see Fig. 5) could be investigated. The forward position was expected to be free of the effects of the expansion at the boattail corner and thus the measurement at this station provides a test of our ability to predict the downstream effects of the boundary-layer/shock-wave interaction which occurs in the region of the ogive-cylinder junction. The most rearward station, only 1.27 cm from the model base, also provides information about the effects of the afterbody shock wave.

The probe travel is controlled by an electric motor within the model which drives a connecting micrometer lead screw. The control allowed positioning of the probe within ±0.03 mm. The position of the probe arm was detected using a linear variable differential transformer which was statically calibrated with an optical cathetometer which provided positioning accuracy of ±0.1 mm. The probe tip was electrically insulated so that wall contact provided a reference position for calibration in the tunnel.

A major concern in using total head probes at transonic speeds is the possibility of flow interference; thus every attempt was made to reduce exposure of the probing mechanism to the main flowfield although some disruption of the base flow is unavoidable. The supersonic region downstream of the boattail corner effectively prevents the upstream propagation of the disturbances caused by the mechanism in wake. This has been verified through photographs of the base flow. No significant upstream effects on the wall static pressure were observed when the probe was in the supersonic region behind the boattail corner. Some upstream propagation from the probe was observed when the probe was in the subsonic flow upstream of the corner but the disturbance was only significant with the probe tip within 1 mm of the model surface. In all cases the wall static pressure measured without the probe mechanism was used to reduce the Pitot probe pressures to Mach numbers. The Mach number profiles were then reduced to velocity by assuming a Crocco temperature-velocity relationship.

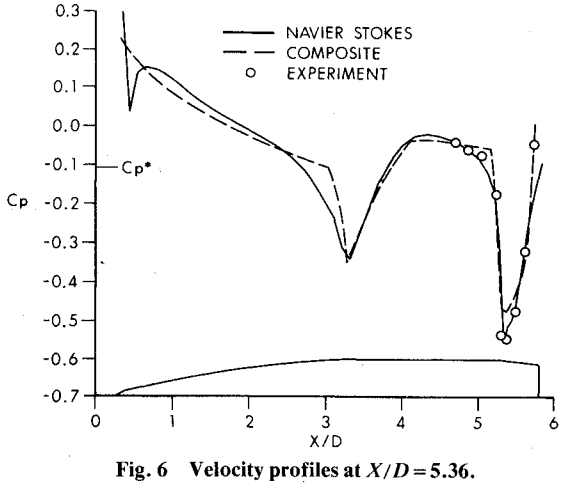

Fig. 6 Velocity profiles at $X/D = 5.36$.

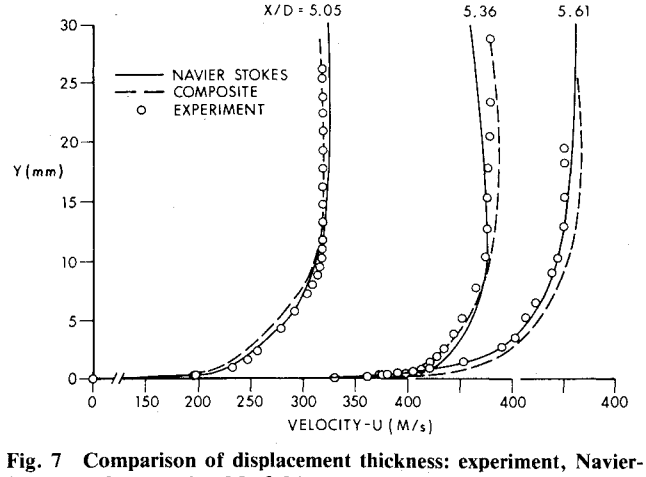

Fig. 7 Comparison of displacement thickness: experiment, Navier-Stokes, and composite; $M = 0.94$.

IX. Results

The results of the experimental investigation are summarized in terms of pressure coefficient distributions given in Table 1 and in terms of the boundary-layer parameters as given in Table 2. All results shown are for $\alpha = 0$ deg, $Re = 13 \times 10^6$/m, and $M = 0.94$ and 0.97.

Comparisons between the two theoretical methods and the measurements are made for surface pressure distribution, velocity profiles, and displacement thickness. Since no experimental measurements were obtained for skin friction a comparison was made between the two theoretical methods only.

A comparison of the surface pressure coefficients for both computational techniques together with the experimental data for $M = 0.94$ is shown in Fig. 6. The overall agreement is generally quite good. The Navier-Stokes results indicate a better agreement with the experimental data in the vicinity of the expansion (negative C_p peak) but fall off slightly at the last point on the boattail. The computational grid contained only 60 points on the body and was severely stretched in the longitudinal direction after the boattail corner, therefore the computation may be less accurate in this region. More significant, however, is that the experimental configuration at the base is not fully modeled in the theoretical methods. During the pressure measurements, the probe mechanism is removed leaving a flat base with a sting of 21% of the base diameter. In contrast, the theoretical solutions are obtained by extending the conical afterbody thereby approximately accounting for the inviscid flowfield but ignoring the free shear layer and recirculation region near the base. Therefore agreement between the computation and experiment cannot be expected in this region. It should be noted again, however, that the supersonic region on the boattail effectively limits the upstream effects of the base flow.

A difference between the two computed results is seen in the vicinity of the two expansion regions (ogive junction and boattail junction). The upstream influence of the corners is seen to be quite extensive in the Navier-Stokes results whereas the composite solution is less affected. The composite solution is composed of an inviscid computation which has not been iterated with the boundary-layer solution. Therefore the effect of a boundary layer has not been accounted for in the composite pressure results, whereas the Navier-Stokes results represent a solution of the entire flowfield. Additionally, the validity of the Navier-Stokes computaton over the entire projectile surface has been shown by Nietubicz[3] to be quite good over a wide Mach number regime.

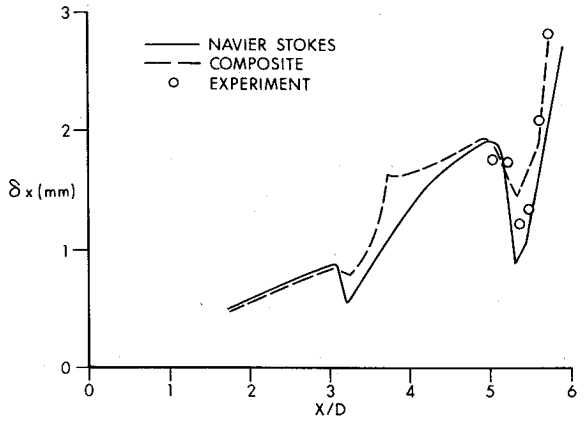

Fig. 8 Experimental comparison of Navier-Stokes, composite, and surface pressure coefficient; $M=0.97$.

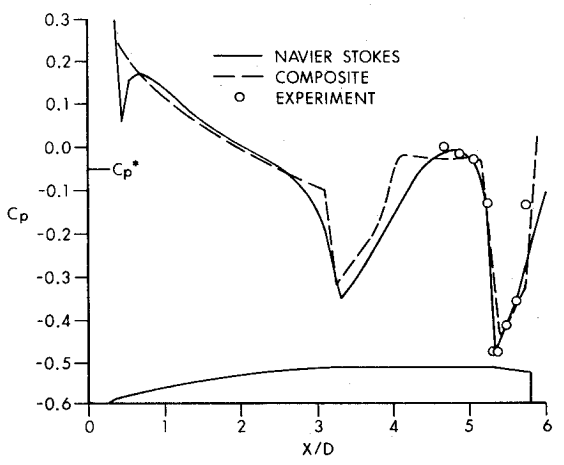

Fig. 9 Velocity profiles at $X/D=5.05$.

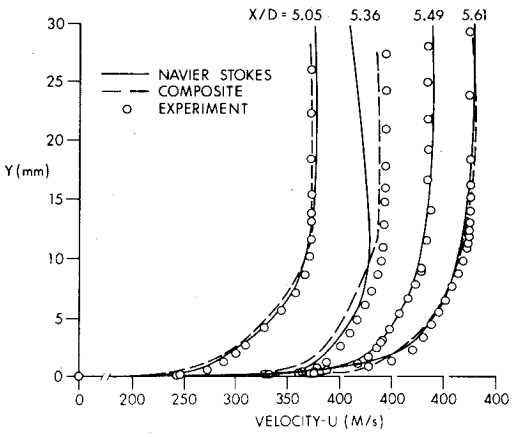

Fig. 10 Comparison of skin friction coefficient vs Navier-Stokes and composite solution techniques.

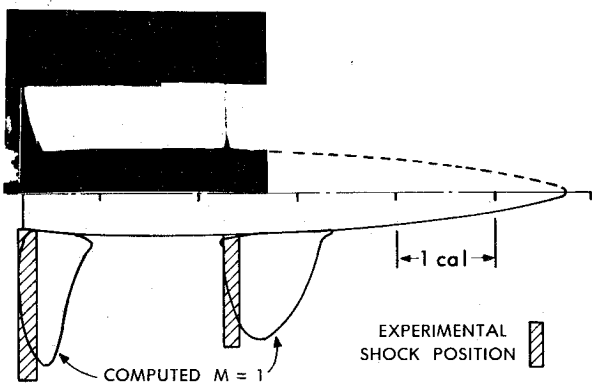

Fig. 11 Boattail shock formation from computer Mach number contours and schlieren photo.

The sharp spike in pressure coefficient which occurs near the nose for the Navier-Stokes results is due to the modeled blunt hemisphere nose shape being computed. Computational experiments for a hemisphere-cone model of similar bluntness at $M=0.95$ have shown that the flow expands locally to supersonic velocities on the nose tip.

Velocity profiles are shown in Fig. 7 for three axial stations at $M=0.94$. Stations $X/D=5.36$ and 5.61 are from previous test results, while the data at $X/D=5.05$ has been obtained from the experiment described in this paper. The Navier-Stokes solution (solid line), composite solutions (dotted line), and experimental values compare very well in all cases with a slight difference being found for the $X/D=5.36$ case. This profile is only 0.06 calibers downstream from the boattail data were reduced using a constant static wall pressure throughout the boundary layer, which could possibly account for the slight differences in the profile comparisons.

A calculation of the displacement thickness was made at all stations where velocity profiles were available. A comparison of the theoretical computations and experimental determination of displacement thickness is shown in Fig. 8. The composite solutions show a rapid rise in displacement thickness at the first shock location and then a gradual increase until the expansion of the second corner is felt which then produces a decrease in the displacement thickness. The Navier-Stokes results on the other hand show a continuous increase in displacement thickness over the cylindrical portion of the model. The experimental results are shown to compare relatively well with the computed values; however, the inability to accurately and consistently determine the boundary-layer edge position velocity in transonic flow makes any comparison suspect. Additionally the solution of Navier-Stokes equations does not rely on the computation of a displacement surface for improved flowfield prediction.

Similar comparisons have been made for $M=0.97$ in order to determine the applicability of these techniques to Mach number variation. The computed and experimental surface pressure coefficients are gain shown in Fig. 9 to compare favorably. The velocity profiles at four axial stations for $M=0.97$ are shown in Fig. 10. The comparison in this case is shown to be good for all stations except $X/D=5.36$, which again is in the expansion region. Slightly downstream of the expansion, however, at $X/D=5.49$, the agreement is again very good. Station $X/D=5.61$ is clearly in the supersonic region at $M=0.97$ as evidenced by schlieren pictures. Disturbances from the probe mechanism are therefore expected to be small in this case. However, for the $M=0.94$ case the supersonic pocket is smaller and interference caused by interaction of the probe and the boattail shock wave is more likely.

Additional features of the computed flowfield can be obtained from the Navier-Stokes computations by plotting the Mach 1 contour line. Figure 11 is a composite picture showing the computed contour together with a schlieren photograph of the boattail region. The photograph is a composite of two schlieren pictures. The upstream region was obtained by translating the model 8 in. downstream in order to bring the ogive-cylinder junction shock wave into view of the camera. Although the wave locations can be determined only within a small region because of optical effects, the results are generally consistent but slightly forward of the predicted Mach 1 lines. The relative movement of the shock waves between $M=0.94$ and 0.97 is consistent with the theoretical prediction.

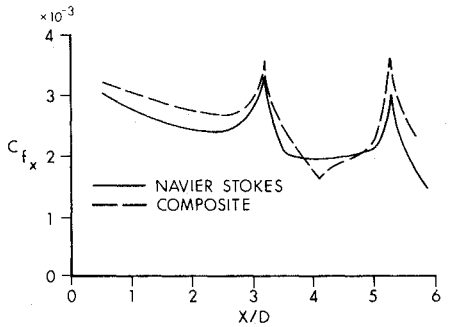

Fig. 12 Comparison of skin friction coefficient between Navier-Stokes and composite solution, $M=0.97$, $\alpha=0$ deg.

A usually severe test of the computational capability is the accurate prediction of the skin friction coefficient. Although the experimental data have not been reduced for comparison, Fig. 12 does show the results for both numerical schemes. The expansion about both corners is shown to produce a rapid increase in the skin friction followed by a rapid decrease after the shock. The relative agreement between these two methods, especially in the presence of multiple shocks, is considered to be quite good.

All computations were performed on the BRL CDC 7600. The Navier-Stokes solutions required approximately 45 min each for convergence, while the composite solution technique ran in approximately 10 min. These times are for the grid size and conditions identified in the body of the paper.

X. Conclusion

The transonic flowfield about a secant-ogive-cylinder boattailed model has been computed using a generalized axisymmetric Navier-Stokes code and a composite shock/boundary-layer interaction technique. The computations have been compared to the experimental data at $M=0.94$ and 0.97 for $\alpha=0$ deg. The results show generally good agreement considering the complex double-shock environment such as exists about this projectile shape.

Additional experimental data are required to fully assess the validity of the computational techniques; however, comparison of the two computational methods with the available data shows generally good agreement. The velocity profile comparisons are exceptionally good considering the severe expansion occurring at the boattail corner. The expansion and rcompression areas are apparent from the C_p curves and the agreement with the data for surface pressure is especially good. A refined grid near the boattail base should improve the Navier-Stokes results in that area.

Navier-Stokes computations have been obtained for the projectile shape considered here at angle of attack and comparisons of these results with the available experimental data and the composite solution technique will be reported in the future.

Acknowledgments

The U.S. Army Research Office supported the measurements reported here under Grant DAAG29-78-G0057. The authors wish to thank R. Tschirschnitz and E. Krueger for the model design and help furnished during the testing.

References

[1] Sturek, W. B., Dwyer, H. A., Kayser, L. D., Nietubicz, C. J., Reklis, R. P., and Opalka, K. O., "Computations of Magnus Effects for a Yawed, Spinning Body of Revolution," *AIAA Journal*, Vol. 16, July 1978, pp. 687-692.

[2] Schiff, L. B. and Sturek, W. B., "Numerical Simulation of Steady Supesonic Flow Over Cone Ogive-Cylinder-Boattail Body," AIAA Paper 80-0066, Jan. 1980.

[3] Nietubicz, C. J., "Navier-Stokes Computations for Conventional and Hollow Projectile Shapes at Transonic Velocities," AIAA Paper 81-1262, Palo Alto, Calif., 1981.

[4] Reklis, R. P., Sturek, W. B., and Bailey, F. L., "Computation of Transonic Flow Past Projectiles at Angle of Attack," U.S. Army Ballistic Research Laboratory/ARRADCOM, Aberdeen Proving Ground, Md., ARBRL-TR-02139, Feb. 1979.

[5] Danberg, J. E., Reklis, R. P., and Inger, G. R., "Pressure Distributions and Boundary Layer Profiles on a Yawed Projectile at Transonic Speeds," Dept. of Mechanical and Aerospace Engineering, University of Delaware, Tech. Rept. 226, April 1979.

[6] Deiwert, G. S., "Numerical Simulation of Three-Dimensonal Boattail Afterbody Flow Field," AIAA Paper 80-1347, July 1980.

[7] Nietubicz, C. J., Pulliam, T. H., and Steger, J. L., "Numerical Solution of the Azimuthal-Invariant Thin-Layer Navier-Stokes Equations," *AIAA Journal*, Vol. 18, Dec. 1980, pp. 1411-1412.

[8] Pulliam, T. H. and Steger, J. L., "On Implicit Finite-Difference Simulations of Three-Dimensonal Flow," *AIAA Journal*, Vol. 18, Feb. 1980, pp. 159-167.

[9] Baldwin, B. S. and Lomax, H., "Thin Layer Approximation and Algebraic Model for Separated Turbulent Flows," AIAA Paper 78-257, Jan. 1978.

[10] Beam, R. and Warming, R. F., "An Implicit Factored Scheme for the Compressible Navier-Stokes Equations," AIAA Paper 77-645, June 1977.

[11] Steger, J. L., Nietubicz, C. J., and Heavey, K. R., "A General Curvilinear Grid Geneation Program for Projectile Configurations," U.S. Army Ballistic Research Laboratory, ARRADCOM, Aberdeen Proving Ground, Md., ARBRL-MR-03142, March 1982.

[12] Dwyer, H. A. and Sanders, B. R., "Magnus Forces on Spinning Supersonic Cones. Part I. The Boundary Layer," *AIAA Journal*, Vol. 14, April 1976, p. 498.

[13] Inger, G. R., "Upstream Influence and Skin Friction in Non-Separating Shock-Turbulent Boundary Layer Interaction," AIAA Paper 80-1411, Colo., July 1980.

[14] Stanewsky, E., Nanandan, M., and Inger, G. R., "Computation of Transonic Flow on Supercritical Airfoils with a Special Solution for Shock-Boundary Layer Interaction," *Computation of Viscous-Inviscid Interactions*, AGARD CP-291, Sept. 1980.

[15] Inger, G. R., "Transonic Shock-Turbulent Boundary Layer Interactions on Spinning Axisymmetric Bodies at Zero Angle of Attack," U.S. Army Ballistic Research Laboratory, ARRADCOM, Aberdeen Proving Ground, Md., ARBRL-TR-02458, Jan. 1983.

[16] Murman, E. M. and Cole, J. D., "Calculation of Plane Steady Transonic Flow," *AIAA Journal*, Vol. 9, Jan. 1971, pp. 114-121.

[17] Walz, A., *Boundary Layers of Flow and Temperature*, MIT Press, Cambridge, Mass., 1969, p. 113.

[18] Reklis, R. P., Danberg, J. E., and Inger, G. R., "Boundary Layer Flows on Transonic Projectiles," AIAA Paper 79-1551, June 1979.